



## Destruction of lithosphere within the north China craton inferred from surface wave tomography

Meijian An, Mei Feng, and Yue Zhao

*Institute of Geomechanics, Chinese Academy of Geological Sciences, Beijing 100081, China (meijianan@yahoo.com.cn)*

*Key Laboratory of Neotectonic Movement and Geohazard, Ministry of Land and Resources of China, Beijing 100081, China*

[1] The north China craton (NCC) is one of the oldest cratons in the world; however, the lithosphere of the craton was destructed during Phanerozoic tectonism and then became tectonically and seismically active. Because the lithospheric structure of this complex craton has not been well studied, the mechanism behind the thinning, transformation, and destruction of the lithosphere remains debated. Using an efficient and scalable 3-D surface wave tomography method, we obtain a high-resolution regional *S* wave velocity model that shows the three-dimensional lithospheric structure of the NCC. In addition, we convert the *S* wave structure to an estimated thermal structure using accepted relationships between *S* wave velocity and temperature. The model images a large upper mantle low-velocity body beneath the eastern NCC, especially beneath the seismically active zone from Tangshan to Xingtai. This body is interpreted to represent hot material or volatiles escaping from the slab edge in the transition zone between the upper and lower mantle. The low-velocity body is a key piece of evidence in demonstrating thermochemical bottom-up erosion/transformation of the overlying cratonic lithosphere, thereby leading to destruction of the lithosphere, which may have occurred during the Cenozoic. This erosion mechanism appears to have had less influence in the western NCC (Ordos block); however, our results reveal a ~130-km-thick lithosphere beneath the present cratonic Ordos block, which is thinner than the ~200 km thickness of the NCC lithosphere during the Paleozoic, as determined from analyses of xenoliths.

**Components:** 9765 words, 7 figures.

**Keywords:** cratonic lithosphere destruction; subduction slab; surface wave tomography; north China.

**Index Terms:** 7218 Seismology: Lithosphere (1236); 8180 Tectonophysics: Tomography (6982, 7270); 8103 Tectonophysics: Continental cratons.

**Received** 15 April 2009; **Revised** 6 July 2009; **Accepted** 10 July 2009; **Published** 26 August 2009.

An, M., M. Feng, and Y. Zhao (2009), Destruction of lithosphere within the north China craton inferred from surface wave tomography, *Geochem. Geophys. Geosyst.*, 10, Q08016, doi:10.1029/2009GC002562.

### 1. Introduction

[2] The north China craton/platform (NCC) (also referred to as the Sino-Korean platform) (Figure 1) is one of the oldest cratons in the world,

preserving crustal remnants as old as 3.8 Ga [Liu *et al.*, 1992]. The craton underwent substantial internal deformation during Phanerozoic tectonism and is divided into three main blocks on the basis of the nature of this deformation: (1) the western part, the

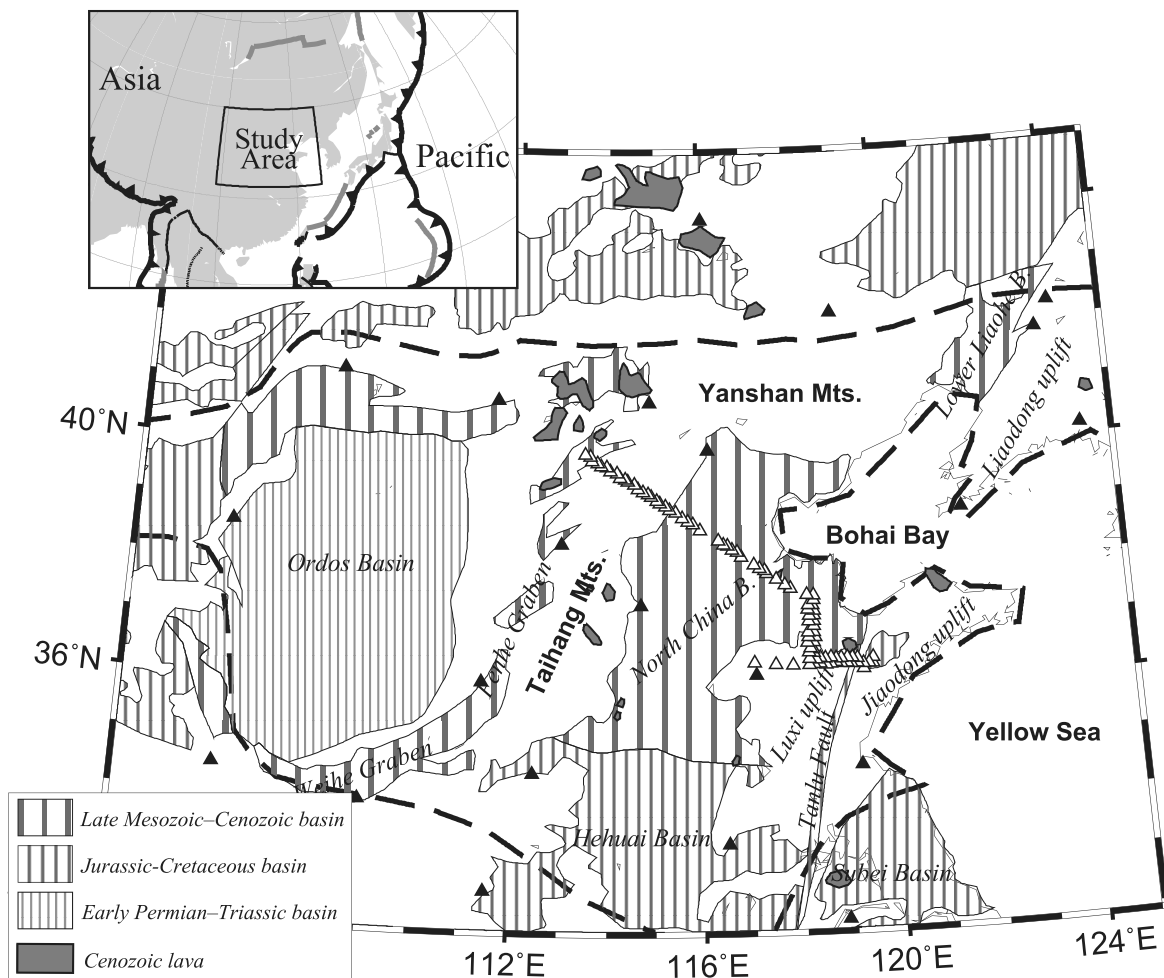


**Figure 1.** Tectonic map of the north China craton. Open triangles are IGGCAS seismic stations, and solid triangles are stations of other networks. Geological data are from *Editorial Committee of Geological Atlas of China* [2002], and the boundary of the north China craton is from *Ren et al.* [1999]. The inset map shows the location of the study area and plate boundaries (thick black lines indicate trenches and areas of underthrusting, thick gray lines indicate spreading ridges, and thin lines indicate transform faults). Plate boundary data are from <http://www.ig.utexas.edu/research/projects/plates>.

Ordos block, is a weakly deformed Paleozoic–Mesozoic basin; (2) the central part, the Shanxi paleouplift, was deformed during the Phanerozoic and records minor magmatism of this age; and (3) the eastern part, the eastern north China block, is intensively deformed and records magmatism from at least the Mesozoic onward [e.g., *Davis et al.*, 2001; *Yang et al.*, 2008; *Hu et al.*, 2009], possibly from the late Paleozoic [*Zhang et al.*, 2009]. Geomorphologically, the western and central parts comprise the Loess Plateau or Highland, upon which the Fen-Wei Graben developed during the late Cenozoic; the eastern part includes the North China and Hehuai basins, and the Bohai Bay depression. The Loess Plateau and the North China Basin are separated by the Taihang Mountains. The basins (i.e., the Bohai Bay depression and the

Fen-Wei Graben) are currently tectonically and seismically active.

[3] Geochemical analyses of xenoliths from eastern north China revealed that the Paleozoic root of the cratonic continental lithosphere, which was characterized by a low geothermal gradient ( $40 \text{ mW/m}^2$ ), was transformed to a young, fertile Phanerozoic subcontinental mantle during the Cenozoic [e.g., *Zhou and Armstrong*, 1982; *Fan et al.*, 1993; *Griffin et al.*, 1998; *Menzies et al.*, 2007]. Since the late Mesozoic, the eastern NCC has been tectonically active, marked by widespread calc-alkaline and intraplate volcanism, and the development of large sedimentary basins and high heat flow ( $>64 \text{ mW/m}^2$ ) [*Griffin et al.*, 1998; *Menzies and Xu*, 1998; *Zheng et al.*, 2001; *Menzies*



*et al.*, 2007]. The thickness of the lithosphere in the eastern NCC has decreased from ~200 km during the Paleozoic [e.g., *Menzies et al.*, 1993; *Griffin et al.*, 1998] to the current-day thickness of ~80 km [e.g., *Chen et al.*, 1991; *Yuan*, 1996; *An and Shi*, 2006]. The current crustal thickness is also much thinner than that during the early Mesozoic [*Xu et al.*, 2006].

[4] Because of its complex evolution from cratonization to reactivation, which caused the observed thinning of the cratonic lithosphere, the NCC is a key region in which to test various geodynamical hypotheses (e.g., continental collision, rifting, and oceanic subduction) that seek to explain why a stable craton was reactivated with coeval magmatism and lithospheric thinning; consequently, many researchers have undertaken studies in the region. For example, the crustal petrology and tectonics of the region have been studied in detail on the basis of geological/geochemical methods [e.g., *Gao et al.*, 2004; *Zhai et al.*, 2004; *Zhao et al.*, 2004; *Wu et al.*, 2006], and information on the deep lithosphere has been retrieved from sparse sites on the basis of analyses of deep level xenoliths and magmatism [e.g., *Zheng et al.*, 2007, 2008; *Gao et al.*, 2008; *Yang et al.*, 2008].

[5] Crustal structure in the NCC is well constrained by two-dimensional deep seismic soundings [e.g., *Wang et al.*, 1993; *Yuan*, 1996; *Zhang et al.*, 1996; *Jia et al.*, 2005] and regional three-dimensional seismic tomography derived from analyses of local earthquakes [e.g., *Zhu and Zeng*, 1990; *Huang and Zhao*, 2004; *Wang et al.*, 2005; *Li et al.*, 2006; *Qi et al.*, 2006]. However, the three-dimensional structure of the lithospheric upper mantle has not been well studied. Although some of the seismic models obtained from teleseismic tomography studies [e.g., *Friederich*, 2003; *Huang et al.*, 2003; *Huang and Zhao*, 2006; *Tian et al.*, 2009] cover the area of the NCC, the results are not at sufficiently high resolution to enable identification of the complex, regional-scale lithospheric structure beneath the NCC at depths of 40–150 km. Because of this lack of high-resolution model, the mechanism that produced lithosphere thinning remains a topic of debate [e.g., *Menzies et al.*, 2007; *Zhai et al.*, 2007], with opinion split between two main hypotheses: (1) lithospheric top-down delamination driven by continental collision/subduction [e.g., *Deng et al.*, 2004; *Gao et al.*, 2004; *Xu et al.*, 2006] and (2) thermal/chemical bottom-up erosion/transformation of the lithosphere driven

by asthenospheric melt [e.g., *Fan et al.*, 2000; *Chen et al.*, 2001; *O'Reilly et al.*, 2001; *Xu*, 2001; *Xu et al.*, 2008]. Detailed descriptions of the potential mechanisms that operated during the tectonic evolution of the NCC can be found in recent reviews [e.g., *Menzies et al.*, 2007; *Zhai et al.*, 2007].

[6] With the aim of exploring the three-dimensional structure of the lithospheric upper mantle and identifying the mechanism of lithospheric thinning/destruction, we present a high-resolution 3-D crustal and upper mantle *S* wave velocity model for the NCC, directly inverted from Rayleigh wave group velocities. The data employed in the present study include not only regional waveforms (with their entire raypaths within the study region) but also teleseismic waveforms (with epicenters that lie outside the study region), as recorded by 110 permanent and temporary seismic stations located in north China in the period up to 2005.

## 2. Data

[7] To improve the path coverage, we collected and measured extensive short-period and broadband data for the period prior to 2005, as recorded by 110 permanent and temporary seismic stations in north China. The stations included 88 temporary stations of the IGGCAS (Institute of Geology and Geophysics, Chinese Academy of Sciences) seismic array, 7 regional seismic stations, 12 permanent NCDSN (New China Digital Seismographic Network) stations, 2 temporary stations operated by IRIS (Incorporated Research Institutions for Seismology), and 1 DSNCC (Digital Seismic Network in Capital Circle) station. The DSNCC station was equipped with short-period seismometers, while the sensors of the IGGCAS stations were equipped with Guralp CMG-3ESPc seismometers with a flat frequency response from 50 Hz to 30 s. Other stations were broadband types.

[8] Rayleigh wave group velocities were measured from vertical component seismograms using a Multiple Filtering Technique (MFT) [*Dziewonski et al.*, 1969] with phase-matched processing by MFT [*Herrin and Goforth*, 1977] to isolate the fundamental mode surface waves. We used the program of *Herrmann and Ammon* [2002], in which instantaneous frequency is preferred, to take into account the spectral amplitude variation [*Nyman and Landisman*, 1977] for each nominal frequency of analysis.

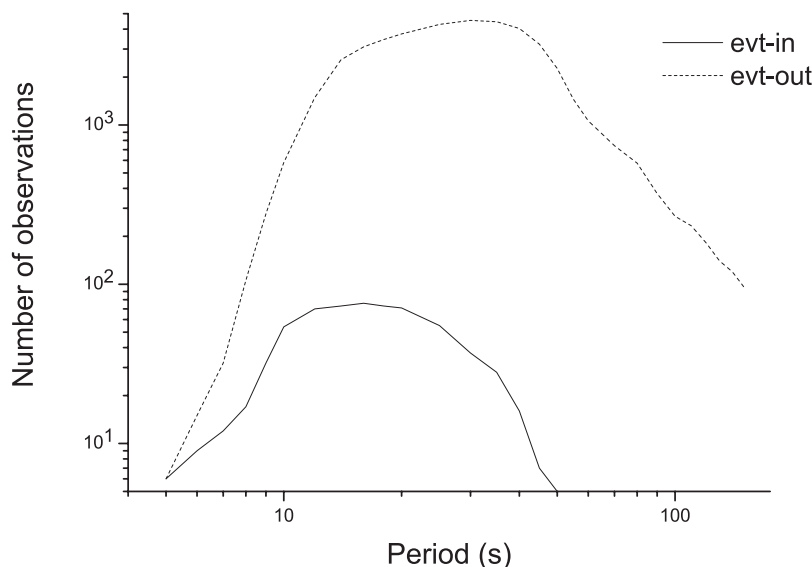


**Figure 2.** Statistical summary of the dispersion observations, i.e., traveltimes for regional paths (evt-in) for which both the epicenter and station were located entirely within the study region and traveltime differences for teleseismic paths (evt-out) for which the epicenter was located outside the study region but the station was located inside.

[9] Because the number and distribution of dispersion measurements can directly influence the reliability of the final inverted  $S$  wave velocity model, we provide a brief description of our measured data set. Figure 2 shows the number of processed Rayleigh wave dispersions for different periods, where the solid line indicates regional (evt-in) observations and the dotted line represents teleseismic (evt-out) observations (a detailed description of the use of teleseismic observations is given in section 3). The numbers of measurements for short periods (<20 s) and long periods (>50 s) are much smaller than those for intermediate periods (20–50 s). The total number of regional observations (solid line in Figure 2) for which the entire paths are within the study region is much less than that of teleseismic observations (dotted line in Figure 2) with epicenters located outside the study region; thus, the teleseismic data are important in improving our inversion results. Figure 3 shows the path density distribution for periods of 20, 50, and 100 s. Most regions within the NCC have a density of more than 20 rays per  $0.25^\circ \times 0.25^\circ$  area ( $\sim 600 \text{ km}^2$ ) for periods shorter than 50 s, but lower densities are recorded in the northwestern and southwestern areas of the study region, especially for periods longer than 100 s.

[10] For most teleseismic events, we used the EHB catalog [Engdahl *et al.*, 1998] to compute the group velocities, although for some regional events for which the estimated primary phase arrivals obtained using the EHB catalog and the IASPEI91

model [Kennett and Engdahl, 1991] are somewhat different from the observed arrivals, we ultimately used the Chinese Seismic Network catalog.

### 3. Methodology

[11] All dispersion curves obtained from each station-to-event ray are directly inverted to construct the 3-D  $S$  wave velocity model. The wave propagation path of the  $k$ th ray can be discretized and its travel time ( $t_k$ ) expressed as

$$t_k = \mathbf{G}_k \cdot \mathbf{S}, \quad (1)$$

where  $\mathbf{G}_k$  is the matrix with the  $k$ th path segment length for each discretized cell and  $\mathbf{S}$  is the surface wave group/phase slowness (reciprocal of velocity) vector, which is the expected tomographic solution obtained by solving equation (1) with the given observed traveltime vector ( $\mathbf{T} = t_1 \dots t_k \dots$ ).

[12] In 1-D regionalized dispersion inversion, the model is parameterized as consisting of horizontally homogeneous layers. In 1-D linearized inversions of dispersion [e.g., Herrmann, 1987; Xia *et al.*, 1999], the regionalized group/phase velocity  $U_R(T_j)$  at the  $j$ th period  $T_j$  for a single cell is expressed by first-order  $S$  wave velocity ( $\Delta\beta$ ) perturbations in each layer ( $i = 1 \dots n$ ) relative to the 1-D reference model ( $\beta_{\text{Ref}}$ ). It is well known that surface wave dispersion is much more sensitive to  $S$  wave velocity than to other parameters (e.g.,  $P$  wave velocity and density);

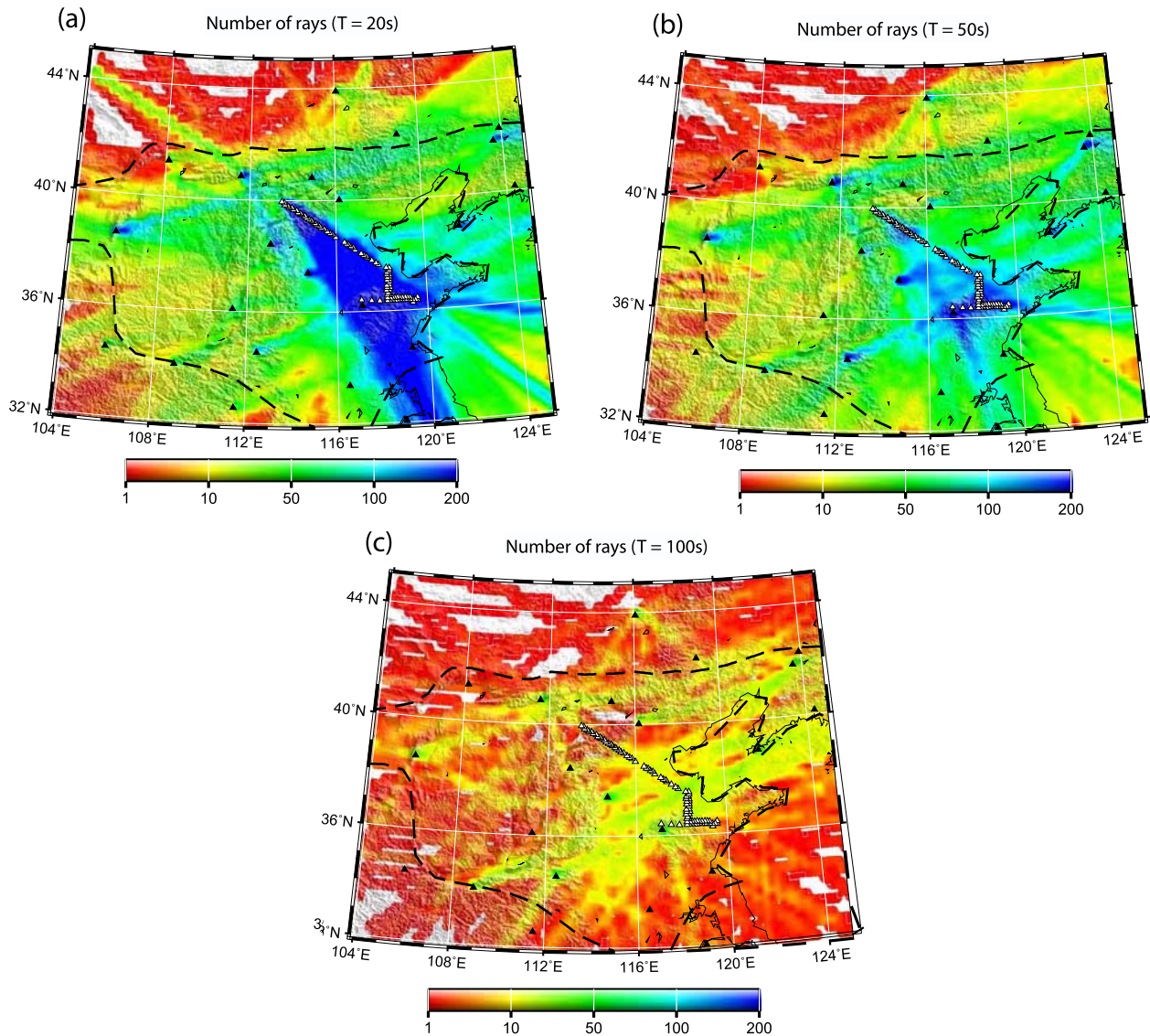


**Figure 3.** Path density of the data at the periods of (a) 20 s, (b) 50 s, and (c) 100 s. Path density is defined as the number of measurements that intersect each  $0.25^\circ \times 0.25^\circ$  cell ( $\sim 600 \text{ km}^2$ ). Path coverage is best in the area between the Taihang Mountains and the Yellow Sea (see Figure 1 for the locations of geographical features and an explanation of other features).

consequently, only  $S$  wave velocity is considered here. The dispersion for the cell can be expressed as

$$U_R(T_j) = U_{\text{Ref}}(T_j) + \sum_{i=1}^n \frac{\partial U}{\partial \beta_i} \Delta \beta_i, \quad (2)$$

where  $\partial U / \partial \beta_i$  is the partial derivative of the group/phase velocity to the  $S$  wave velocity of the  $i$ th layer of the reference model, and  $U_{\text{Ref}}(T_j)$  is the dispersion of the reference model. Given the reference model and  $U_R(T_j)$ , perturbations of the  $S$  wave velocity vector ( $\Delta \beta$ ) can be determined by solving equation (2), and the

new solution ( $\beta_{\text{Ref}} + \Delta \beta$ ) can be taken as the new reference model. By iteratively perturbing the previous reference model, the final model is obtained when a good fit to the dispersion curve is achieved. By carrying out such inversions separately for each cell, the final 3-D model is constructed by assembling the inverted 1-D profiles of all cells. This represents the basic approach in obtaining a 3-D  $S$  wave velocity model in traditional surface wave dispersion tomography.

[13] The basic assumption that underlies the linearized inversion using equation (2) is that the



partial derivative  $\partial U/\partial\beta_i$  is constant. In this case,  $\partial S/\partial\beta_i$  (the partial derivative of group/phase slowness) is also constant, and the following equation is valid:

$$S_R(T_j) = S_{\text{Ref}}(T_j) + \sum_{i=1}^n \frac{\partial S}{\partial\beta_i} \Delta\beta_i, \quad (3)$$

where  $S_{\text{Ref}}(T_j)$  is the group/phase slowness of the reference model. Given the reference model and  $U_R(T_j)(= 1/S_R(T_j))$ , the perturbations of  $S$  wave velocity ( $\Delta\beta$ ) can also be determined by solving equation (3).

[14] Replacing the vector  $\mathbf{S}$  in equation (1) with that from equation (3), equation (1) becomes

$$t_k = \mathbf{A}_k \cdot \mathbf{B} + c_k, \quad (4)$$

where  $\mathbf{A}_k$  is a coefficient matrix deduced from operations between the matrix  $\mathbf{G}_k$  and all partial derivatives  $\partial S/\partial\beta_i$ ,  $\mathbf{B}$  is the vector of 3-D  $S$  wave velocity perturbations to be determined, and  $c_k$  is a constant from the combination of  $\mathbf{G}_k$  and  $S_{\text{Ref}}$ . For all paths and all periods, we can then obtain the travel time vector ( $\mathbf{T}$ ) in the following matrix form:

$$\mathbf{T} = \mathbf{A} \cdot \mathbf{B} + \mathbf{C}, \quad (5)$$

where  $\mathbf{C}(= c_1, \dots, c_k, \dots)$  is a constant vector. By solving equation (5), we obtain the 3-D  $S$  wave velocity perturbations directly from the observed dispersions.

[15] The above discussion considered only regional observations for which both the events and stations were located within the study region; however, given a slightly modified equation, it is also possible to use the method for teleseismic observations and stations or events located outside the study region.

[16] For a pair of close rays (e.g., the  $m$ th and  $k$ th rays) from a common epicenter/station located outside the study region, if the outside parts of the two rays are sufficiently close that the structures beneath the outside parts can be considered the same, the arrival time difference between the two close rays can be taken as that contributed by the part inside the study region,  $\Delta t_{m-k} = (\mathbf{A}_m - \mathbf{A}_k)\mathbf{B} + (c_m - c_k)$ . For many pairs of such close rays, the time difference can be expressed as

$$\Delta\mathbf{T} = \Delta\mathbf{A} \cdot \mathbf{B} + \Delta\mathbf{C}, \quad (6)$$

which is similar to equation (5). By solving equation (6), we also obtain the 3-D  $S$  wave velocity perturbations directly from the observed teleseismic dispersions.

[17] Because equations (5) and (6) are commonly ill posed, a priori constraints are necessary, and the final inversion equation becomes

$$\begin{pmatrix} \mathbf{T} - \mathbf{C} \\ \Delta\mathbf{T} - \Delta\mathbf{C} \\ \mathbf{0} \end{pmatrix} = \begin{pmatrix} \mathbf{A} \\ \Delta\mathbf{A} \\ \lambda\nabla \end{pmatrix} \cdot \mathbf{B}, \quad (7)$$

where  $\nabla$  represents the first-order spatial gradient of the model, serving as smoothness for the final 3-D  $S$  wave velocity model, and  $\lambda$  is a weighting factor to balance between fitting the travel times and smoothing the model. Equation (7) can be used to determine the 3-D  $S$  wave velocity directly and jointly from regional and teleseismic observations. The above method is more efficient and scalable than the conventional two-step surface wave tomography (which involves period-by-period 2-D tomographic inversions for regionalized dispersions followed by cell-by-cell inversions of regionalized dispersions for 1-D  $S$  wave–velocity profiles), and any 3-D physical constraints are easily introduced into the inversion, which is difficult to achieve using the conventional two-step method. A detailed introduction to this method is given by M. Feng and M. An (Lithospheric structure of the Chinese mainland from a single-step inversion of regional and teleseismic surface wave, submitted to *Journal of Geophysical Research*, 2009).

[18] The most important aspect of a seismological study is to retrieve petrologic or geodynamical information (e.g., temperature) from seismic velocities; however, seismic velocity is nonlinearly related to mineral composition and physical conditions (e.g., pressure/depth and temperature). Previous studies [e.g., *Goes et al.*, 2000] have demonstrated that upper mantle temperature can be nonlinearly inverted from seismic velocities on the basis of laboratory measurements of density and elastic moduli for various mantle minerals at high temperatures and pressures; similar analyses [e.g., *Goes et al.*, 2000; *Röhm et al.*, 2000; *Goes and Van der Lee*, 2002; *Cammarano et al.*, 2003; *Shapiro and Ritzwoller*, 2004; *An and Shi*, 2006] have been widely applied in studies of the upper mantle thermal structure.

[19] A previous seismic-thermal analysis of the Chinese continent [*An and Shi*, 2006] revealed that



the base of the seismic lithosphere corresponds closely to the base of the seismic–thermal lithosphere, thereby demonstrating the validity of the seismic–thermal analysis method. Here, we converted the upper mantle  $S$  wave velocities at positions deeper than 50 km into temperatures, using the off-cratonic composition, as employed by An and Shi [2006, 2007]. Because the effect of mineral composition can give velocity anomalies of <1% for the shallow mantle and would therefore be difficult to be resolved in seismic tomography [Goes et al., 2000], spatial variations in composition were not considered in the conversion. A temperature uncertainty of  $\sim 150^\circ\text{C}$  may exist in the conversion [Goes et al., 2000; An and Shi, 2006, 2007].

[20] The presence of fluids (e.g., melt and water) results in a marked lowering of seismic velocities [Hirth and Kohlstedt, 1996; Karato and Jung, 1998; Goes et al., 2000; Avseth et al., 2005]; however, there exists no model that shows the distribution of melt and fluids in the upper mantle beneath the study area. Therefore, we did not consider the effects of melt and fluids in the conversion from velocity to temperature. If fluid-affected velocities are interpreted in terms of temperatures, temperature would be overestimated. Thus, the mantle temperature estimated in our study should be taken as the upper bound, and if the converted temperature for the upper mantle is anomalously high, a possible reason for the overestimate may be the existence of fluids (melt or water).

#### 4. Model Parameters and Resolution Tests

[21] Given the dominance of short-period data in our group velocity data set, the 3-D  $S$  wave velocity model is parameterized with grid spacings of  $0.25^\circ$  in both latitude and longitude and with a vertical layer thickness of 5 km down to 45 km depth and 10 km to 300 km depth. It is preferable to consider a regional 3-D crustal and upper mantle  $S$  wave velocity as the reference model, but no such model has been developed.

[22] The Moho depth in the NCC varies between about 30 and 40 km [Bassin et al., 2000; Jia and Zhang, 2005; Zheng et al., 2006], similar to that in the IASPEI91 model (35 km [Kennett and Engdahl, 1991]). Therefore, we first used the 1-D IASPEI91 model as the reference model in the inversion, and then a 3-D reference model for which the

crustal  $S$  wave velocities are interpolated from the CRUST2.0 model [Bassin et al., 2000] and the upper mantle  $S$  wave velocities from IASPEI91. Ray propagation paths are traced on the basis of Snell's law. The  $S$  wave velocity anomaly patterns obtained from the two reference models are similar, indicating that the resulting models are stable and minimally dependent on the initial model; accordingly, the results obtained using IASPEI91 as a reference model are considered reliable, and are shown below.

[23] Structural heterogeneity along the raypath is an important factor in the 1-D inversion of surface wave dispersion [Kennett and Yoshizawa, 2002; An and Assumpção, 2005, 2006]; however, it is less important in 3-D surface wave tomography. Propagation effects such as refraction along a heterogeneous path can result in uncertainties in observations [Kennett and Yoshizawa, 2002]; however, the wave propagation effects can be averaged out if the path coverage (path density, and path azimuth and path distance distribution) is satisfactory in 3-D tomography. In addition, we performed ray tracing under group velocity maps from general 2-D group velocity tomography inversion, and the test results showed that the improvement in the result obtained for the region beneath the NCC with ray tracing can be ignored, possibly because of the largely homogeneous crustal thickness in the NCC. When the path structure beneath a cell is highly heterogeneous, the average structure information beneath the cell can be inverted by introducing a smoothing constraint [An and Assumpção, 2005, 2006]. In the present study, the paths are traced and the inversions are constrained by lateral and vertical smoothing, meaning that path heterogeneity has little influence on our inversion results.

[24] Checkerboard tests performed using synthetic data can be used to determine the resolution of the inverted models, and the resolution derived from checkerboard tests are resolution upper bound because checkerboard tests do not take into account the inherent limitations on resolution from the finite Fresnel zone. Here, we use 3-D checkers. Figure 4 shows the input and output  $S$  wave velocity structures in the checkerboard resolution test with checker sizes of  $2^\circ \times 2^\circ \times 5$  layers ( $2^\circ$  in longitude and latitude, and 5 layers in depth (Figure 4a)) and  $4^\circ \times 4^\circ \times 7$  layers (Figure 4b), respectively. The input model has a  $\pm 7\%$  velocity variation relative to the IASPEI91 model at all depths. The test results show that the  $2^\circ \times 2^\circ$  checkers (Figure 4a) are well recovered between

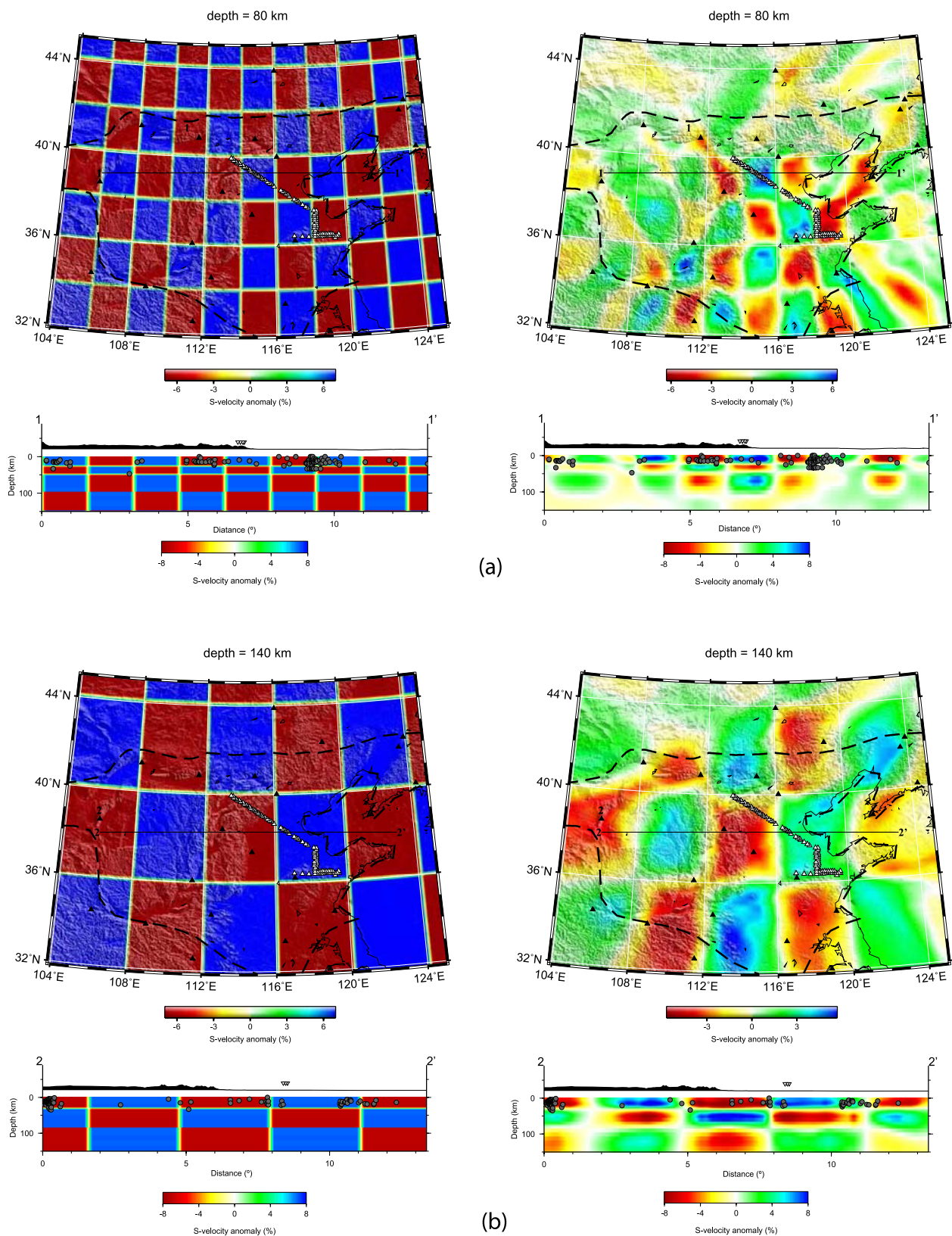


**Figure 4.** Lateral and vertical  $S$  wave velocity slices of the results of a checkerboard test. The sizes of the 3-D checkers are (a)  $2^\circ \times 2^\circ \times 5$  layers (longitude and latitude  $2^\circ$ , five layers vertically) and (b)  $4^\circ \times 4^\circ \times 7$  layers. Circles in the cross sections represent earthquake hypocenters. See Figure 1 for an explanation of other features.



112°E and 120°E down to 100 km depth. Given that the average resolution is equal to half of the recovered checker dimension [Lebedev and Nolet, 2003], the average lateral resolution in our study region is  $\sim 1^\circ$  ( $\sim 100$  km) down to 100 km depth, and the vertical resolution is  $\sim 10$  km down to 50 km depth and  $\sim 25$  km down to 100 km (see Figure 4a). The  $4^\circ \times 4^\circ$  checkers (Figure 4b) are well recovered beneath the entire NCC; the average lateral resolution down to 200 km depth is  $\sim 2^\circ$  ( $\sim 200$  km), and the vertical resolution is  $\sim 35$  km. The regions with  $\sim 1^\circ$  lateral resolution (Figure 4a) in the crust and lithospheric upper mantle ( $<100$  km) correspond directly to regions with a raypath coverage density higher than 30 rays per  $0.25^\circ \times 0.25^\circ$  cell for 20–50 s dispersions (Figures 3a and 3b). Throughout the entire NCC, the sublithospheric upper mantle ( $>\sim 100$  km depth) with  $2^\circ$  lateral resolution (Figure 4b) corresponds to regions with good raypath coverage density for 100 s dispersion measurements, as shown in Figure 3c.

## 5. Results

[25] Given a vertical resolution of  $\sim 10$  km within the crust, the 5-km-depth map reflects the average  $S$  wave velocity structures at depths down to  $\sim 10$  km. In this map (Figure 5a), low-velocity anomalies indicate thick sediment and strong depression. As expected, young basins have lower  $S$  wave velocities. For example, the Cenozoic North China Basin has the lowest-velocity anomaly; the late Mesozoic–Cenozoic Hehuai Basin has relatively low velocities, and the Ordos block has weak/no low velocities. The North China and Hehuai basins are tectonically active and contain a great thickness of sediment; for example, Holocene sediments in north China with  $>30$  m thickness are mainly found in the north China and western Hehuai basins [Zeng *et al.*, 1989]. The Yanshan Mountains and Luxi uplift show a high-velocity anomaly. The anomaly pattern near Beijing ( $39^\circ$ – $41^\circ$ N and  $114$ – $119^\circ$ E) is the same as the  $P$  wave velocity anomaly in sediment ( $\sim 2$  km) analyzed from deep seismic sounding profiles [Jia *et al.*, 2005].

[26] The average present-day thicknesses of crust and lithosphere in the NCC are  $\sim 35$  km [Bassin *et al.*, 2000; Jia and Zhang, 2005; Zheng *et al.*, 2006] and  $\sim 80$  km [An and Shi, 2006], respectively; consequently, the  $S$  wave velocity slice at 60 km depth (Figure 5b) shows general structures of the lithospheric upper mantle, revealing a low-velocity

anomaly beneath the area east of Xingtai (XTI in Figure 5b) in the North China Basin. Interestingly, the Bohai Bay depression shows a high-velocity anomaly.

[27] A horizontal slice at a depth of 110 km (Figure 5c) shows the sublithospheric structure of the NCC. At this depth, a NE-SW trending low-velocity belt is imaged beneath the North China Basin, extending from Tangshan (TSH) to Xingtai (XTI). The low-velocity belt is located along an active seismic zone, along which the disastrous Xingtai earthquakes ( $M_s$  6.8 and 7.2) occurred in March of 1966 and along which the well-known Tangshan earthquake ( $M_s = 7.9$ ) occurred on 27 July 1976. The low-velocity belt is marked by high heat flow ( $>2.0$  HFU) [Menzies *et al.*, 2007, and references therein].

[28] To the southeast of the low-velocity belt, there exists a parallel high-velocity belt that extends northeastward to the high-velocity Bohai Bay. The sharp velocity transition between the two belts indicates a marked difference in temperature and composition. An interesting feature of the horizontal slice is that although the Bohai Sea is underlain by strongly depressed thin crust, the upper mantle lithosphere is cold and thick. A low-velocity anomaly is also found beneath the boundary between the North China and Hehuai basins, which is covered by a great thickness of Holocene sediments, similar to the area to the northeast of Xingtai.

[29] The vertical profiles show both  $S$  wave velocity and temperature anomalies. The temperatures were converted from upper mantle  $S$  wave velocities using the off-cratonic composition, following An and Shi [2006, 2007]; temperatures at depths greater than 50 km are shown in the lower cross section of Figure 6. Profile a–a' (Figures 5a and 6a) is oriented parallel to the short E–W trending station array (along the profile q–q') operated by IGGCAS, and crosses the Tanlu Fault zone, which is a first-order Cenozoic tectonic feature in East Asia. The  $P$  and  $S$  receiver functions (P-RFs and S-RFs, respectively) of the E–W station array were analyzed and projected onto profile a–a' by Chen *et al.* [2006, 2008], and their obtained seismic lithosphere bottoms are marked as dashed lines (P-RFs) and solid lines (S-RFs) in profiles a–a' and q–q' (Figures 6a and 6b).

[30] Figure 6a reveals a complex lithosphere velocity structure in profile a–a', and the lithosphere base in our model is different from the receiver

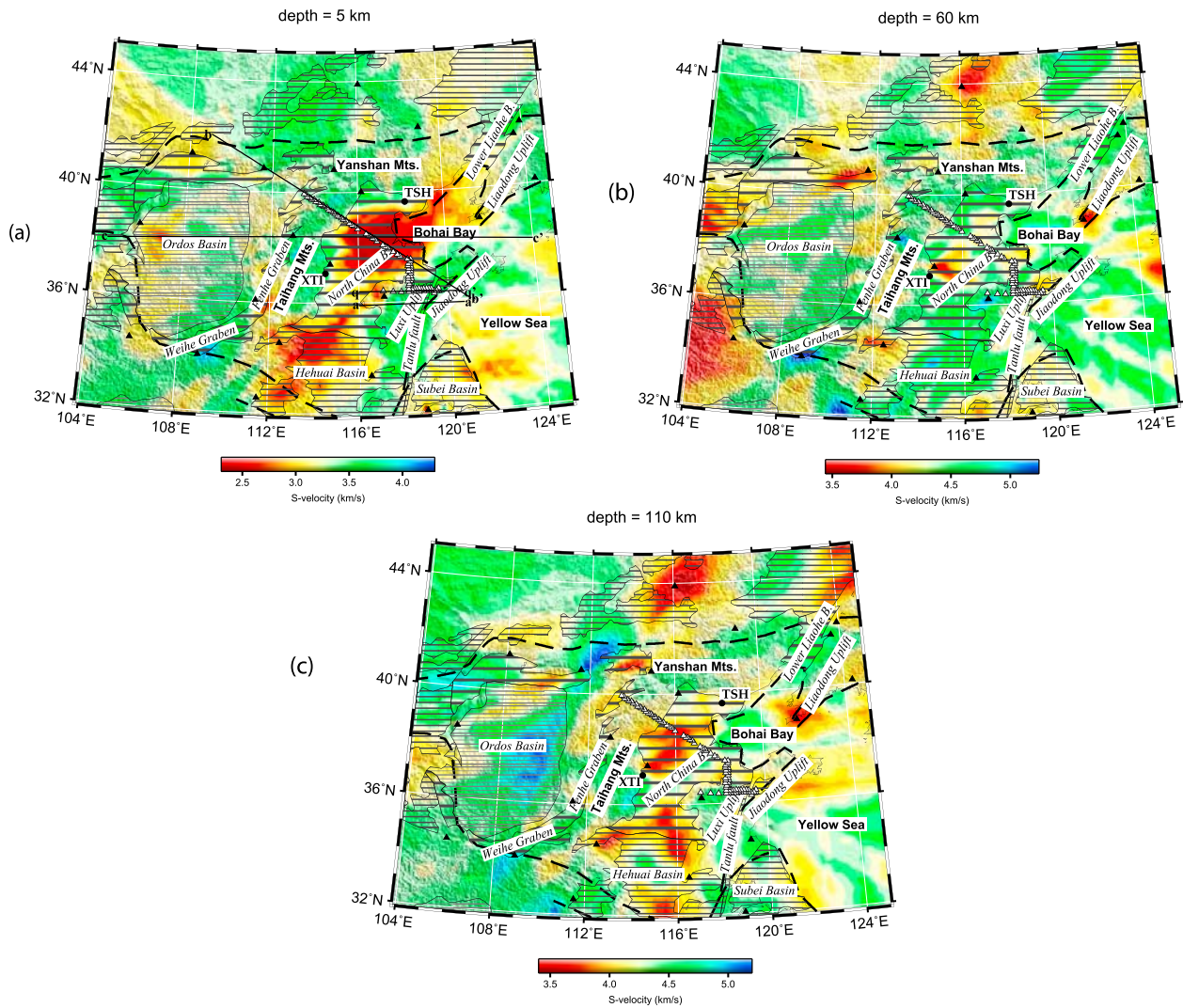


**Figure 5.** Horizontal cross sections through the  $S$  wave velocity model at depths of (a) 5 km, (b) 60 km, and (c) 110 km. The boundary of the north China craton (thick dashed line) also demarcates the region outside of which data coverage is poor. Solid circles are cities (XTI, Xingtai; TSH, Tangshan).

function (RF) results. In contrast, along profile  $q-q'$ , located along the E–W station array (Figure 5a), our results for the region beneath the Jiaodong (JD) uplift reveal a thin lithosphere of  $\sim 80$  km in thickness, consistent with the RF results. Accordingly, we focus on comparing the model in profile  $q-q'$  with the previous RF results. Despite the above similarity, our result along profile  $q-q'$  shows some marked differences with the RF results (e.g., the lithosphere base beneath the Luxi uplift in our result is different from that in the RF results). Overall, our result shows a sharp increase in lithosphere thickness from the Jiaodong uplift to the Luxi uplift, yet previous RF-based studies show only a slight increase in lithosphere thickness. In fact, the previous RF results for the Luxi uplift are less reliable than those for the Jiaodong

uplift because the stations located upon the Luxi uplift are sparsely distributed, and the results derived from P-RF and S-RF analyses are similar for the Jiaodong uplift but different for the Luxi uplift [Chen *et al.*, 2006, 2008]. Given that the Tanlu Fault is a large-scale fault that cuts across the northeastern Eurasian continent [Xu *et al.*, 1987; Wang *et al.*, 2000], the sharp variation in the lithosphere base detected across the fault is more reasonable than a smooth variation. A recently developed  $P$  wave velocity model [Tian *et al.*, 2009] showed variations in velocity across the Tanlu Fault that are similar to the variations obtained in the present study. The above comparison demonstrates that our inversion is reliable and yields a high-resolution result for the lithospheric upper mantle. Along the profile  $q-q'$ , the low

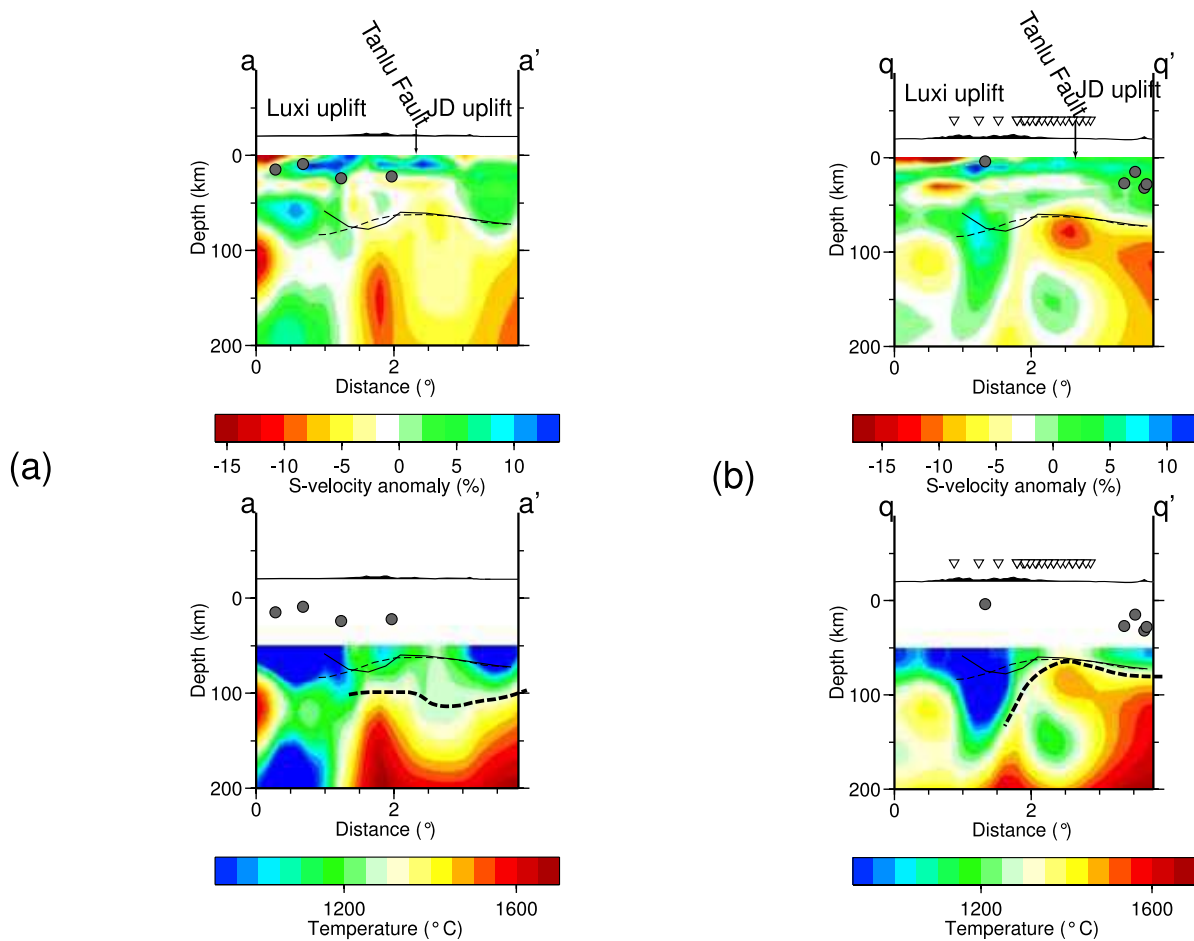


**Figure 6.** Vertical cross sections (a) a–a′, (b) q–q′, (c) b–b′, and (d) c–c′ through the *S* wave velocity model. The locations of the cross sections are shown in Figure 5a. Inverted triangles show the locations of IGGCAS stations. Earthquakes are indicated by circles. The vertical black bar in profile c–c′ marks the location of an abrupt anomaly in *S* wave velocity and temperature. The thick dashed lines represent the base of the lithosphere, as estimated from the temperatures. In profiles a–a′ and q–q′, thin dashed and solid lines represent the lithosphere bottom, as estimated from *P* receiver functions [Chen *et al.*, 2006] and *S* receiver functions [Chen *et al.*, 2008], respectively.

velocity observed beneath the Tanlu Fault to depths below 50 km indicates that the fault may extend down to the asthenosphere.

[31] Profile b–b′ (Figure 6c) is located along a NW–SE trending station array operated by IGGCAS. Zheng *et al.* [2006] carried out a detailed RF study on the structure beneath this array to a depth of 50 km. The Moho depth estimated by Zheng *et al.* [2006] varies from ~30 km in the east to 40 km beneath the Taihang Mountains in the west. The lithosphere thickness in our results (profile b–b′) shows the same increase from east to west as seen in crustal thickness. The lowest velocities/highest temperatures below 80 km depth are observed beneath the active Tangshan–Xingtai (TSH–XTI) seismic zone, and the shape of the high-temperature anomaly resembles a plume. The lithosphere

beneath the Tanlu Fault is thinner than in surrounding areas.

[32] Profile c–c′ (Figure 6d) extends from the Ordos block in the west to Bohai Bay in the east. The *S* wave velocity and temperature models reveal a number of interesting features. First, the lithosphere beneath the Ordos block is generally thicker (~130 km) than that beneath other parts of the NCC, and the lithosphere thickness is highly variable beneath the central and eastern NCC. Given the absence of Mesozoic–Cenozoic magmatism within the Ordos Basin, the thicker lithosphere beneath the Ordos block shows that it remains cratonic and stable; accordingly, the thickness of ~130 km indicates that the original cratonic lithosphere thickness was possibly much thinner than previously estimated (~200 km), the typical thick-

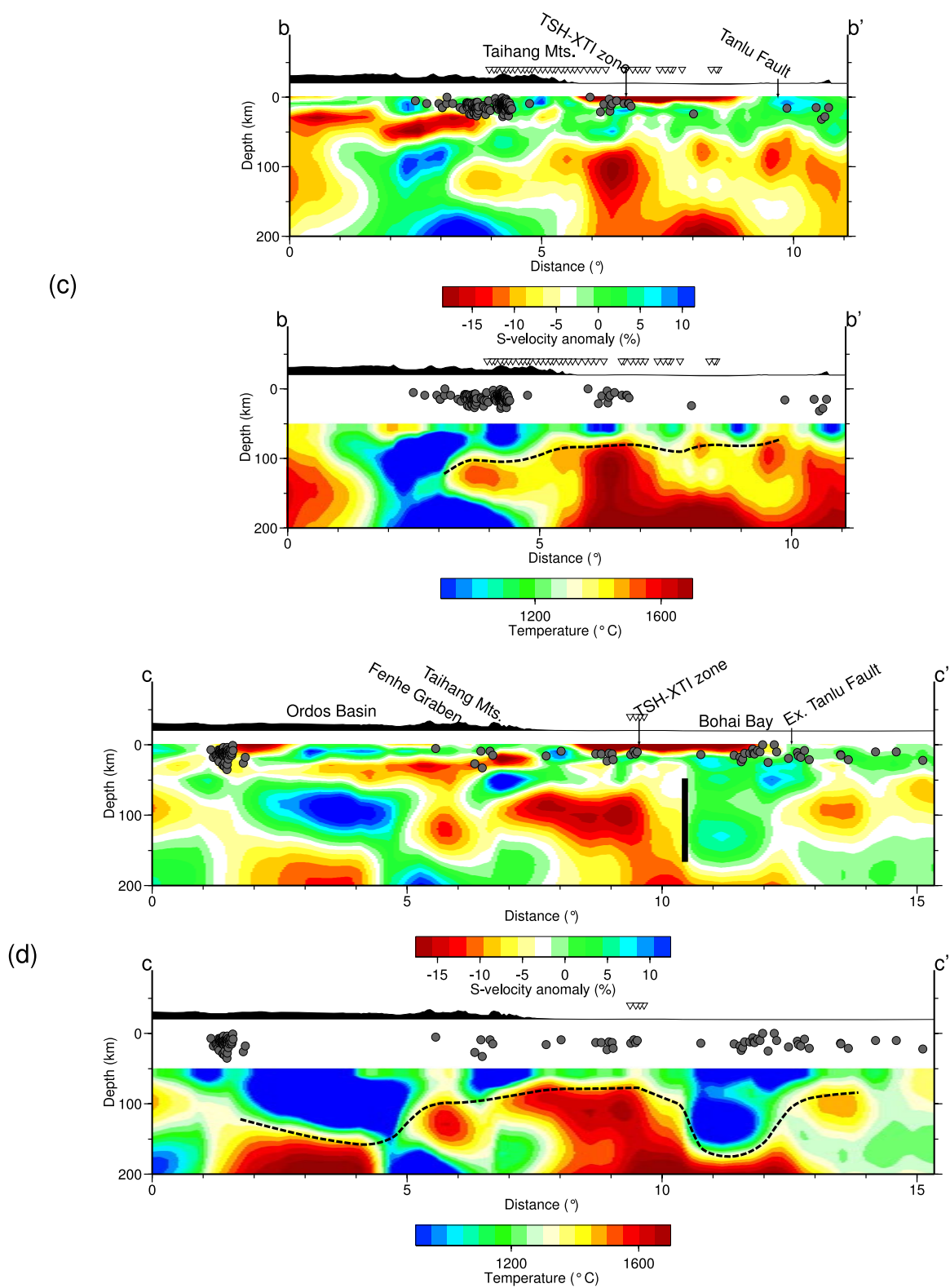


Figure 6. (continued)



ness of cratonic lithosphere [Sleep, 2005]. Second, the lithosphere and sublithosphere beneath the Fenhe Graben record a low-velocity/high-temperature anomaly. Third, an obvious vertical boundary (marked by the black vertical bar in Figure 6d) between an area of low velocities to the west and high velocities to the east is observed at depths of 50–150 km, to the east of the active Tangshan–Xingtai seismic zone. The nature of the boundary indicates a sharp change in the mechanical, petrological, and thermal properties of the upper mantle, suggesting in turn that the neighboring blocks experienced contrasting, rapid geodynamic processes. Fourth, a plume-like high-temperature anomaly is clearly imaged between the Taihang Mountains and the Tangshan–Xingtai seismic zone, extending upward to 70 km depth; the anomaly extends from the low-velocity anomaly beneath the Fenhe Graben.

[33] We did not consider the effects of melts/fluid and composition in the conversion from seismic velocity to temperature. The effect of composition can generate a temperature anomaly of  $<150^\circ$  for the shallow mantle [Goes *et al.*, 2000; An and Shi, 2006], and the presence of melts/fluid (or hot flow) can generate a high-temperature anomaly ( $>300^\circ$ ) like in the plume-like hot body beneath the Tangshan–Xingtai seismic zone (Figure 6d). Therefore, this image (Figure 6d) may indicate that a plume-like hot body intruded to the northwest of the Tangshan–Xingtai seismic zone, eroding the overlying lithosphere. The sharp velocity boundary (black vertical bar in Figure 6d) indicates that the intrusion of the hot body occurred rapidly and recently. Finally, the thickness of the lithosphere shows a sharp change across the northward extrapolation of the Tanlu Fault, indicating that the fault extends down to the asthenosphere. Most of the above features are discussed in detail below.

## 6. Discussion

### 6.1. Cenozoic Sublithospheric Erosion

[34] Deep earthquakes ( $\sim 600$  km depth) have been recorded beneath northeastern China, demonstrating the existence of a deep level subducting slab. Although no such deep earthquakes have been recorded in the NCC, it has been suggested that the NCC may also be influenced by the subducting slab. Seismic tomographic images [e.g., van der Hilst *et al.*, 1991; Fukao *et al.*, 1992; van der Hilst *et al.*, 1997; Fukao *et al.*, 2001; Pysklywec and Ishii, 2005; Huang and Zhao, 2006] reveal that the

westward subducting oceanic slab extends from the surface to the transition zone, changing to a sub-horizontal orientation above 660 km depth, beneath eastern China.

[35] Figure 7b shows a  $P$  wave velocity model along  $39^\circ$  latitude (simplified from Huang and Zhao [2006, Figure 8b]), along a similar path to cross section  $c-c'$  (Figures 6d and 7a). The cross sections in Figures 7a and 7b have a latitudinal difference of  $<1^\circ$ , smaller than the lateral resolutions of the models at depths  $>100$  km. Therefore, the cross sections can be taken as intersecting the same structure. The  $P$  wave velocity model shows that low  $P$  wave velocities near the slab's western edge, in the transition zone between the lower and upper mantle, possibly connect with the plume-like hot body (Figure 7a) beneath the North China Basin, as the low  $P$  wave velocities (Figure 7b) are nearly continuous at depths of 100–800 km beneath the North China Basin.

[36] The slab edge, in the transition zone beneath eastern north China, is located  $\sim 1800$  km from the present-day trench zone. For a convergence rate of  $\sim 90$  km/Ma for the Pacific Plate and  $\sim 50$  km/Ma for the Philippine Plate relative to the Eurasian Plate (based on the model HS3-NUVEL1A [Gripp and Gordon, 2002]), movement of the subducting slab from the trench zone to the present-day edge would require  $\sim 20$  Ma for the Pacific Plate and  $\sim 36$  Ma for the Philippine Plate. Honda and Yuen [2001] showed that a 100-km-thick hot intrusion takes  $\sim 50$  Ma to attain a thermal steady state via conduction. For a wet subducting oceanic slab that is heated simultaneously at its lower and upper boundaries, accompanied by both conduction and partial melting/geochemical assimilation, less than  $\sim 50$  Ma is required to attain a thermal steady state. Therefore, a period of 20–36 Ma seems reasonable for a  $\sim 100$ -km-thick oceanic lithospheric slab to become mostly heated, accompanied by partial melting and fluid release, and to arrive at the present-day slab edge, located close to the area beneath the North China Basin (Figure 7b).

[37] In terms of horizontal movement of the slab at the transition zone between the lower and upper mantle, the hot and relatively buoyant material beneath the base of the cold slab would be confined because of obstruction by the slab itself. However, the heated material in the west to the slab edge (Figure 7b) could become too weak to continue to obstruct the upwelling of accumulated buoyant material at the slab base. Therefore, the melt released from the slab base could concentrate

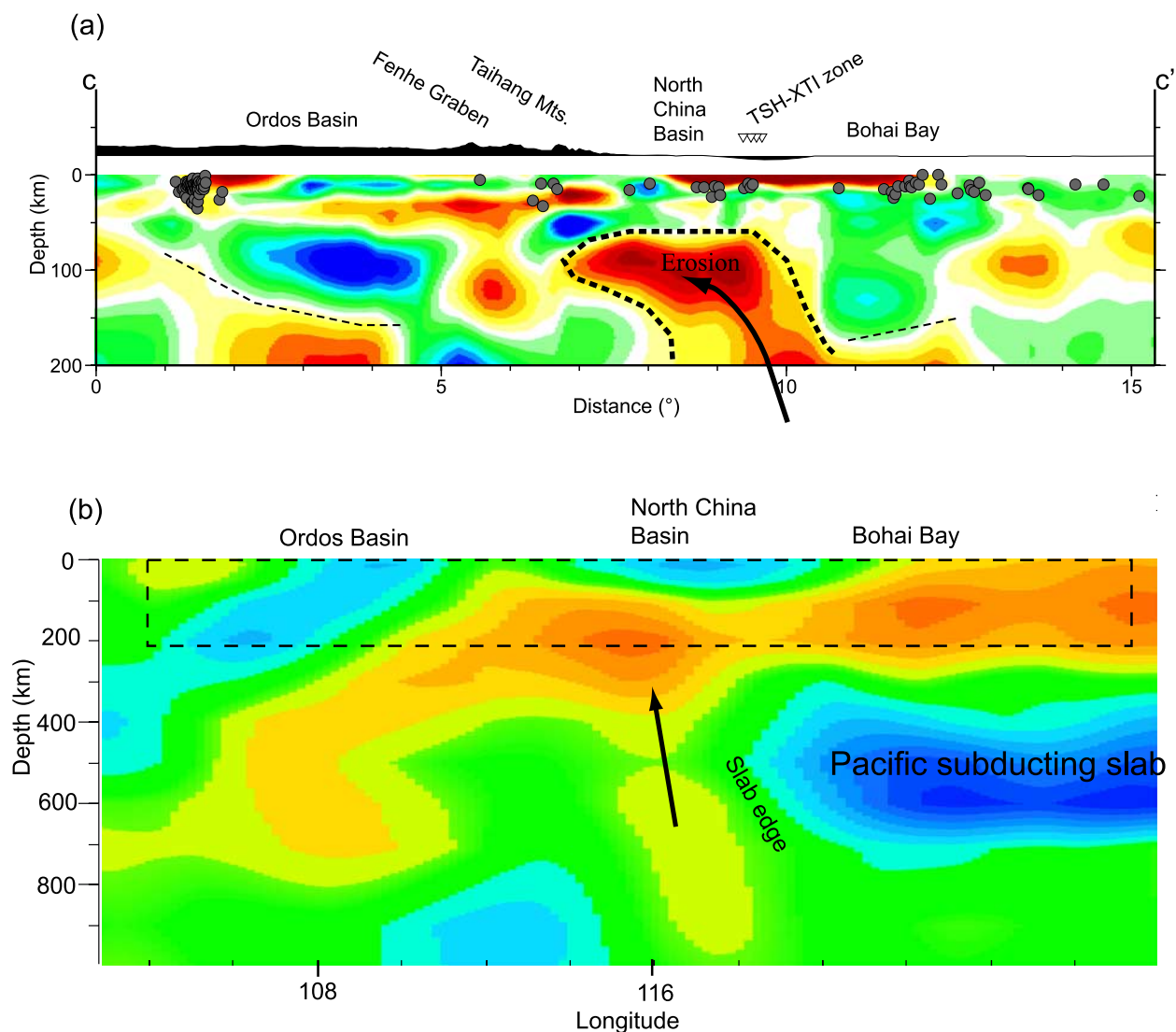


**Figure 7.** Model depicting hot material ascending from the mantle transition zone. (a) Model in which the  $S$  wave velocity is the same as that in Figure 6d. (b)  $P$  wave velocity model along  $39^\circ$  latitude (simplified from Huang and Zhao [2006, Figure 8b]). The cross sections in Figures 7a and 7b have a latitudinal difference of  $<1^\circ$ , smaller than the lateral resolutions in the two models at depths of  $>100$  km. Therefore, the cross sections can be taken as crossing the same structure. The thin dashed line in Figure 7a marks the base of the protolithosphere, and the thick dashed line marks the extent of an intrusion of an upper mantle hot body that ascended from the slab edge. The dashed rectangle in Figure 7b shows the location of Figure 7a. Arrows indicate the movement direction of melt.

to the west to the slab edge, forming a low-velocity body at the mantle transition zone, similar to that shown in Figure 7b, as imaged by Huang and Zhao [2006]. The hot, low-velocity material at the mantle transition zone is hotter and more buoyant than the overlying asthenosphere, and escapes upward to the base of the lithosphere. Water and harzburgite derived from the stagnant slab have been found beneath northeastern China [Ichiki et al., 2006]. The mixing of upper mantle material with the escaping materials, especially fluids, can cause a reduction in the solidus temperature in the

asthenosphere/lithosphere [e.g., Iwamori, 1992; Tatsumi and Eggins, 1995; Ichiki et al., 2006]. The upwelling of hot asthenospheric mantle material, triggered by partial melting of enriched subcontinental lithospheric mantle, can impregnate and refertilize the refractory protolith of a cratonic lithospheric root, eroding the base of the lithosphere. Lithosphere-asthenosphere interaction can modify the lithospheric root and lead to its replacement by more fertile material [Menzies et al., 1993; Lee et al., 1996; Griffin et al., 1998; Pearson, 1999]. Petrological and geochemical evidences



[Wilde *et al.*, 2003; Chen *et al.*, 2005, 2007] revealed that magmatism within the eastern NCC at 135–127 Ma was related to the upwelling of asthenosphere, caused in turn by subduction of the paleo-Pacific Plate.

[38] Our seismic model shows an upper mantle low-velocity (hot) body (Figure 7a) above the low *P* wave velocities near the edge of the stagnant Pacific slab. On the basis of the above discussion, the hot body may represent material generated in the overlying asthenospheric mantle because of the infiltration of fluids/melts from the slab or material that directly escaped near the slab edge. In this context, our model supports the above erosion model in explaining the destruction/thinning of the NCC lithosphere which may have happened in the Cenozoic. Replacement or erosion beneath the eastern north China craton could have destroyed the cratonic lithosphere root, leading to thermal activity (e.g., high heat flow of >2.0 HFU) [Menzies *et al.*, 2007, and references therein] and pronounced depressions in the North China Basin, which can still be observed today.

[39] The development of large Mesozoic and Cenozoic basins in the eastern NCC was concentrated in two stages (Jurassic–Cretaceous and Cretaceous–present), possibly related to the subduction of the paleo-Pacific and Pacific plates, respectively [Griffin *et al.*, 1998]. It is clear that the asthenospheric upwelling discussed above can be related to the latter of the above periods of basin formation. Petrological and geochemical data [Wilde *et al.*, 2003; Chen *et al.*, 2005, 2007] revealed that magmatism within the eastern NCC at 135–127 Ma (the beginning of the latter period of basin formation) was linked to the upwelling of asthenosphere caused by subduction of the paleo-Pacific Plate. Tertiary–Holocene volcanism in the eastern part of the north China craton and large-scale subsidence in the area around Bohai Bay suggest that the effects of the process of lithosphere destruction are continuing to be observed today [Yang *et al.*, 2008].

[40] Most previous studies on the effects of a subducting slab on overlying asthenosphere/lithosphere have generally focused on areas close to trench–arc systems (e.g., Pacific island arcs and marginal seas or back-arc basins) [e.g., Poli and Schmidt, 2002; Arcay *et al.*, 2005; Bebout, 2007; Tsuji *et al.*, 2008]. The NCC is located ~1800 km from the trench–arc system, yet we imaged a low-velocity/hot body just above the slab edge in the mantle transition zone and beneath the destroyed

cratonic lithosphere. Therefore, hot and buoyant material escaping from the mantle transition zone near the slab edge is potentially an important dynamical source that influences intraplate tectonics (e.g., the Tangshan–Xingtai seismic zone in the NCC (Figure 7a)). Within eastern north China, this tectonism resulted by hot upwelling postdated Mesozoic tectonism [e.g., Davis *et al.*, 2001; Zhao *et al.*, 2004].

[41] The lithosphere beneath the Ordos block, the western NCC, and Bohai Bay (but not that beneath the North China Basin (Figure 7a)) were not eroded by the hot upwelling mentioned above, and the lithosphere base (i.e., the bottom of the upper mantle seismic lid) can be found down to depths of ~130 km. In these regions, the lithosphere is much thinner (~130 km) than normal cratonic lithosphere (~200 km) [Sleep, 2005]. Geochemical and isotopic data derived from mantle xenoliths within Paleozoic diamond-bearing kimberlites [Griffin *et al.*, 1998] located close to the Tanlu Fault revealed the existence of a thick (~200 km) cratonic lithosphere in the Paleozoic, at least as late as the middle Ordovician. This thickness is often taken as the pre-Mesozoic thickness of lithosphere in the NCC. If the thickness of the Paleozoic lithosphere estimated on the basis of xenoliths is also valid for the western NCC and the Ordos block, a mechanism other than asthenospheric upwelling is required to explain the extensive post-Paleozoic thinning of the lithosphere in these regions.

## 6.2. Earthquake Probability Indicated by Deep Structure

[42] Because the lithosphere beneath the Tangshan–Xingtai seismic zone was eroded by upper mantle upwelling, the crust along the zone is deeply depressed. Of course, crustal stress is concentrated at the two ends of the seismic zone (the areas in and around Tangshan and Xingtai), which will have large strain gradients. This dynamical background means that the areas of (or close to) Xingtai and Tangshan have a higher probability of large earthquakes than do areas in the middle of the seismic zone. This interpretation explains why great earthquakes of the past have occurred in the areas of Xingtai and Tangshan in the North China Basin.

## 7. Conclusions

[43] The north China craton records a complex history from cratonization to reactivation, which



caused thinning of the cratonic lithosphere. Our *S* wave velocity model imaged an upper mantle low-velocity (hot) body beneath the North China Basin. The melt in the asthenospheric hot body has possibly impregnated and refertilized the refractory protolith within the lithosphere root over a long period. Therefore, the low-velocity image may support the mechanism of thermal/chemical “bottom-up” erosion/transformation of lithosphere in the north China craton, which has thinned the lithosphere since the late Mesozoic, at the very least during the Cenozoic. However, this erosion mechanism had only a minor influence on the western NCC and the Ordos block, and our model reveals a lithosphere thickness of ~130 km beneath these areas, much less than that previously estimated for the Paleozoic NCC lithosphere (~200 km) on the basis of analyses of xenoliths; therefore, a mechanism other than thermal/chemical “bottom-up” erosion/transformation is required to explain extensive post-Paleozoic thinning of the lithosphere in these regions.

## Acknowledgments

[44] We are grateful to the China Earthquake Data Center, IGGCAS, and IRIS for making available seismic data analyzed in this study. This work was supported by the National Natural Science Foundation of China (grants NSFC-40674058 and 40504011) and the National Basic Research Program of China (grant 2006CB403501). We are grateful to Rob van der Hilst and Suzanne O'Reilly for their rigorous and constructive suggestions that significantly improved the quality of the manuscript. We thank Douglas A. Wiens for his constructive comments and suggestions, and we also thank two anonymous reviewers for careful reviews of the manuscript. Figures 1–7 were generated using the Generic Mapping Tools [Wessel and Smith, 1991].

## References

- An, M., and M. S. Assumpção (2005), Effect of lateral variation and model parameterization on surface wave dispersion inversion to estimate the average shallow structure in the Paraná Basin, *J. Seismol.*, *9*, 449–462, doi:10.1007/s10950-005-2841-8.
- An, M., and M. S. Assumpção (2006), Crustal and upper mantle structure in intracratonic Paraná Basin, SE Brazil, from surface wave dispersion using genetic algorithm, *J. South Am. Earth Sci.*, *21*(3), 173–184, doi:10.1016/j.jsames.2006.03.001.
- An, M., and Y. Shi (2006), Lithospheric thickness of the Chinese continent, *Phys. Earth Planet. Inter.*, *159*, 257–266, doi:10.1016/j.pepi.2006.08.002.
- An, M., and Y. Shi (2007), 3D crustal and upper-mantle temperature of the Chinese continent, *Sci. China, Ser. D*, *50*(10), 1441–1451.
- Arcay, D., et al. (2005), Numerical simulations of subduction zones: Effect of slab dehydration on the mantle wedge dynamics, *Phys. Earth Planet. Inter.*, *149*(1–2), 133–153, doi:10.1016/j.pepi.2004.08.020.
- Avseth, P., et al. (2005), *Quantitative Seismic Interpretation: Applying Rock Physics Tools to Reduce Interpretation Risk*, 359 pp., Cambridge Univ. Press, Cambridge, U. K.
- Bassin, C., et al. (2000), The current limits of resolution for surface wave tomography in North America, *Eos Trans. AGU*, *81*(48), Fall Meet. Suppl., S12A-03.
- Bebout, G. E. (2007), Metamorphic chemical geodynamics of subduction zones, *Earth Planet. Sci. Lett.*, *260*(3–4), 373–393, doi:10.1016/j.epsl.2007.05.050.
- Cammarano, F., et al. (2003), Inferring upper-mantle temperatures from seismic velocities, *Phys. Earth Planet. Inter.*, *138*(3–4), 197–222, doi:10.1016/S0031-9201(03)00156-0.
- Chen, B., et al. (2005), Zircon U-Pb geochronology and geochemistry of the Mesozoic magmatism in the Taihang Mountains and other places of the north China craton, with implications for petrogenesis and geodynamic setting, *Acta Petrol. Sin.*, *21*(1), 13–24.
- Chen, B., et al. (2007), Origin of the Mesozoic magmatism in the north China craton: Constraints from petrological and geochemical data, *Geol. Soc. Publ.*, *280*(1), 131–151.
- Chen, G.-Y., et al. (1991), Three-dimensional crust and upper mantle structure of the north China region, *Acta Geophys. Sin.*, *34*(2), 172–181.
- Chen, L., et al. (2006), A thinned lithospheric image of the Tanlu Fault Zone, eastern China: Constructed from wave equation based receiver function migration, *J. Geophys. Res.*, *111*, B09312, doi:10.1029/2005JB003974.
- Chen, L., et al. (2008), Distinct lateral variation of lithospheric thickness in the northeastern north China craton, *Earth Planet. Sci. Lett.*, *267*, 56–68, doi:10.1016/j.epsl.2007.11.024.
- Chen, S., et al. (2001), Thermal and petrological structure of the lithosphere beneath Hannuoba, Sino-Korean Craton, China: Evidence from xenoliths, *Lithos*, *56*(4), 267–301, doi:10.1016/S0024-4937(00)00065-7.
- Davis, G. A., et al. (2001), Mesozoic tectonic evolution of the Yanshan fold and thrust belt, with emphasis on Hebei and Liaoning provinces, northern China, in *Paleozoic and Mesozoic Tectonic Evolution of Central and Eastern Asia: From Continental Assembly to Intracontinental Deformation*, edited by M. S. Hendrix and G. A. Davis, *Mem. Geol. Soc. Am.*, *194*, 171–198.
- Deng, J. F., et al. (2004), A new model for the dynamic evolution of Chinese lithosphere: ‘Continental roots–plume tectonics’, *Earth Sci. Rev.*, *65*, 223–275, doi:10.1016/j.earscirev.2003.08.001.
- Dziewonski, A. M., et al. (1969), A technique for analysis of transient seismic signals, *Bull. Seismol. Soc. Am.*, *59*(1), 427–444.
- Editorial Committee of Geological Atlas of China (2002), *Geological Atlas of China*, Geol. Publ. House, Beijing.
- Engdahl, E. R., et al. (1998), Global teleseismic earthquake relocation with improved travel times and procedures for depth determination, *Bull. Seismol. Soc. Am.*, *88*, 722–743.
- Fan, W., et al. (1993), Nature and processes of the lower lithosphere of the southeast China coast, *Geotecton. Metal.*, *17*(1), 23–30.
- Fan, W. M., et al. (2000), On and off the north China craton: Where is the Archaean Keel?, *J. Petrol.*, *41*(7), 933–950, doi:10.1093/petrology/41.7.933.
- Friederich, W. (2003), The S-velocity structure of the East Asian mantle from inversion of shear and surface waveforms, *Geophys. J. Int.*, *153*, 88–102, doi:10.1046/j.1365-246X.2003.01869.x.



- Fukao, Y., et al. (1992), Subducting slabs stagnant in the mantle transition zone, *J. Geophys. Res.*, *97*(B4), 4809–4822, doi:10.1029/91JB02749.
- Fukao, Y., et al. (2001), Stagnant slabs in the upper and lower mantle transition region, *Rev. Geophys.*, *39*(3), 291–323, doi:10.1029/1999RG000068.
- Gao, S., et al. (2004), Recycling lower continental crust in the north China craton, *Nature*, *432*, 892–897, doi:10.1038/nature03162.
- Gao, S., et al. (2008), Recycling deep cratonic lithosphere and generation of intraplate magmatism in the north China craton, *Earth Planet. Sci. Lett.*, *270*(1–2), 41–53, doi:10.1016/j.epsl.2008.03.008.
- Goes, S., and S. Van der Lee (2002), Thermal structure of the North American uppermost mantle inferred from seismic tomography, *J. Geophys. Res.*, *107*(B3), 2050, doi:10.1029/2000JB000049.
- Goes, S., et al. (2000), Shallow mantle temperatures under Europe from P and S wave tomography, *J. Geophys. Res.*, *105*(B5), 11,153–11,169, doi:10.1029/1999JB900300.
- Griffin, W. L., et al. (1998), Phanerozoic evolution of the lithosphere beneath the Sino-Korean craton, in *Mantle Dynamics and Plate Interactions in East Asia*, edited by M. F. J. Flower et al., pp. 107–126, AGU, Washington, D. C.
- Gripp, A. E., and R. G. Gordon (2002), Young tracks of hotspots and current plate velocities, *Geophys. J. Int.*, *150*, 321–361, doi:10.1046/j.1365-246X.2002.01627.x.
- Herrin, E., and T. Goforth (1977), Phase-matched filters: Application to the study of Rayleigh waves, *Bull. Seismol. Soc. Am.*, *67*, 1259–1275.
- Herrmann, R. B. (1987), *Computer Programs in Seismology*, Saint Louis Univ., Saint Louis, Mo.
- Herrmann, R. B., and C. J. Ammon (2002), *Computer Programs in Seismology—Surface Waves, Receiver Functions and Crustal Structure*, Saint Louis Univ., Saint Louis, Mo.
- Hirth, G., and D. L. Kohlstedt (1996), Water in the oceanic upper mantle: Implications for rheology, melt extraction and the evolution of the lithosphere, *Earth Planet. Sci. Lett.*, *144*, 93–108, doi:10.1016/0012-821X(96)00154-9.
- Honda, S., and D. A. Yuen (2001), Interplay of variable thermal conductivity and expansivity on the thermal structure of oceanic lithosphere, *Geophys. Res. Lett.*, *28*(2), 351–354, doi:10.1029/2000GL012096.
- Hu, J., et al. (2009), Early Mesozoic deformations of the eastern Yanshan thrust belt, northern China, *Int. J. Earth Sci.*, doi:10.1007/s00531-009-0417-5, in press.
- Huang, J., and D. Zhao (2004), Crustal heterogeneity and seismotectonics of the region around Beijing, China, *Tectonophysics*, *385*(1–4), 159–180, doi:10.1016/j.tecto.2004.04.024.
- Huang, J., and D. Zhao (2006), High-resolution mantle tomography of China and surrounding regions, *J. Geophys. Res.*, *111*, B09305, doi:10.1029/2005JB004066.
- Huang, Z., et al. (2003), Rayleigh wave tomography of China and adjacent regions, *J. Geophys. Res.*, *108*(B2), 2073, doi:10.1029/2001JB001696.
- Ichiki, M., et al. (2006), Water content and geotherm in the upper mantle above the stagnant slab: Interpretation of electrical conductivity and seismic P wave velocity models, *Phys. Earth Planet. Inter.*, *155*(1–2), 1–15, doi:10.1016/j.pepi.2005.09.010.
- Iwamori, H. (1992), Degree of melting and source composition of Cenozoic basalts in southwest Japan: Evidence for mantle upwelling by flux melting, *J. Geophys. Res.*, *97*(B7), 10,983–10,995.
- Jia, S.-X., and X.-K. Zhang (2005), Crustal structure and comparison of different tectonic blocks in north China, *Chin. J. Geophys.*, *48*(3), 672–683.
- Jia, S.-X., et al. (2005), Three-dimensional crustal gridded structure of the capital area, *Chin. J. Geophys.*, *48*(6), 1316–1324.
- Karato, S., and H. Jung (1998), Water, partial melting and the origin of the seismic low velocity and high attenuation zone in the upper mantle, *Earth Planet. Sci. Lett.*, *157*, 193–207, doi:10.1016/S0012-821X(98)00034-X.
- Kennett, B. L. N., and E. R. Engdahl (1991), Traveltimes for global earthquake location and phase identification, *Geophys. J. Int.*, *105*, 429–465, doi:10.1111/j.1365-246X.1991.tb06724.x.
- Kennett, B. L. N., and K. Yoshizawa (2002), A reappraisal of regional surface wave tomography, *Geophys. J. Int.*, *150*, 37–44, doi:10.1046/j.1365-246X.2002.01682.x.
- Lebedev, S., and G. Nolet (2003), Upper mantle beneath Southeast Asia from S velocity tomography, *J. Geophys. Res.*, *108*(B1), 2048, doi:10.1029/2000JB000073.
- Lee, D.-C., et al. (1996), Melt enrichment of shallow depleted mantle: A detailed petrological, trace element and isotopic study of mantle-derived xenoliths and megacrysts from the Cameroon Line, *J. Petrol.*, *37*(2), 415–441, doi:10.1093/ptrology/37.2.415.
- Li, Z.-W., et al. (2006), Seismic tomography and velocity structure in the crust and upper mantle around Bohai Sea area, *Chin. J. Geophys.*, *49*(3), 797–804.
- Liu, D. Y., et al. (1992), Remnants of > or = 3800 Ma crust in the Chinese part of the Sino-Korean Craton, *Geology*, *20*(4), 339–342, doi:10.1130/0091-7613(1992)020<0339:ROMCIT>2.3.CO;2.
- Menzies, M. A., and Y.-G. Xu (1998), Geodynamics of the north China craton, in *Mantle Dynamics and Plate Interactions in East Asia*, *Geodyn. Ser.*, vol. 27, edited by M. F. J. Flower et al., pp. 155–165, AGU, Washington, D. C.
- Menzies, M. A., et al. (1993), Palaeozoic and Cenozoic lithoproses and the loss of >120 km of Archaean lithosphere, Sino-Korean craton, China, *Geol. Soc. Spec. Publ.*, *76*, 71–81.
- Menzies, M., et al. (2007), Integration of geology, geophysics and geochemistry: A key to understanding the north China craton, *Lithos*, *96*, 1–21, doi:10.1016/j.lithos.2006.09.008.
- Nyman, D. C., and M. Landisman (1977), The display equalized filter for frequency-time analysis, *Bull. Seismol. Soc. Am.*, *67*, 393–404.
- O'Reilly, S. Y., et al. (2001), Are lithospheres forever? Tracking changes in subcontinental lithospheric mantle through time, *GSA Today*, *11*(4), 4–10, doi:10.1130/1052-5173(2001)011<0004:ALFTCI>2.0.CO;2.
- Pearson, D. G. (1999), The age of continental roots, *Lithos*, *48*(1–4), 171–194, doi:10.1016/S0024-4937(99)00026-2.
- Poli, S., and M. W. Schmidt (2002), Petrology of subducted slabs, *Annu. Rev. Earth Planet. Sci.*, *30*(1), 207–235, doi:10.1146/annurev.earth.30.091201.140550.
- Pysklywec, R. N., and M. Ishii (2005), Time dependent subduction dynamics driven by the instability of stagnant slabs in the transition zone, *Phys. Earth Planet. Inter.*, *149*, 115–132, doi:10.1016/j.pepi.2004.08.019.
- Qi, C., et al. (2006), 3-D P and S wave velocity structures and their relationship to strong earthquakes in the Chinese capital region, *Chin. J. Geophys.*, *49*(3), 805–815.
- Ren, J., et al. (1999), The tectonics of China from a global view—A guide to the tectonic map of China and adjacent regions, 32 pp., Geol. Pub. House, Beijing.
- Röhm, A. H. E., et al. (2000), Thermal structure of continental upper mantle inferred from S-wave velocity and surface heat



- flow, *Earth Planet. Sci. Lett.*, *181*, 395–407, doi:10.1016/S0012-821X(00)00209-0.
- Shapiro, N. M., and M. H. Ritzwoller (2004), Thermodynamic constraints on seismic inversions, *Geophys. J. Int.*, *157*, 1175–1188, doi:10.1111/j.1365-246X.2004.02254.x.
- Sleep, N. H. (2005), Evolution of the continental lithosphere, *Annu. Rev. Earth Planet. Sci.*, *33*, 369–393, doi:10.1146/annurev.earth.33.092203.122643.
- Tatsumi, Y., and S. Eggins (1995), *Subduction Zone Magmatism*, Blackwell Sci., London.
- Tian, Y., et al. (2009), Seismic imaging of the crust and upper mantle beneath the north China craton, *Phys. Earth Planet. Inter.*, *172*(3–4), 169–182, doi:10.1016/j.pepi.2008.09.002.
- Tsuji, Y., et al. (2008), Tomographic evidence for hydrated oceanic crust of the Pacific slab beneath northeastern Japan: Implications for water transportation in subduction zones, *Geophys. Res. Lett.*, *35*, L14308, doi:10.1029/2008GL034461.
- van der Hilst, R. D., et al. (1991), Tomographic imaging of subducted lithosphere below northwest Pacific island arcs, *Nature*, *353*, 37–42, doi:10.1038/353037a0.
- van der Hilst, R. D., et al. (1997), Evidence for deep mantle circulation from global tomography, *Nature*, *386*, 578–584, doi:10.1038/386578a0.
- Wang, C. Y., et al. (1993), A study on fine crustal structure in Xingtai earthquake area based on deep seismic reflection profiling, *Chin. J. Geophys.*, *36*(4), 445–452.
- Wang, F.-Y., et al. (2005), Fine tomographic inversion of the upper crust 3-D structure around Beijing, *Chin. J. Geophys.*, *48*(2), 359–366.
- Wang, X., et al. (2000), *On Tan-Lu Fault Zone* (in Chinese with English abstract), 362 pp., Geol. Publ. House, Beijing.
- Wessel, P., and W. H. F. Smith (1991), Free software helps map and display data, *Eos Trans. AGU*, *72*, 411, doi:10.1029/90EO00319.
- Wilde, S. A., et al. (2003), Mesozoic crust-mantle interaction beneath the north China craton: A consequence of the dispersal of Gondwanaland and accretion of Asia, *Geology*, *31*(9), 817–820, doi:10.1130/G19489.1.
- Wu, F.-Y., et al. (2006), The chemical-temporal evolution of lithospheric mantle underlying the north China craton, *Geochim. Cosmochim. Acta*, *70*, 5013–5034, doi:10.1016/j.gca.2006.07.014.
- Xia, J., et al. (1999), Estimation of near-surface shear-wave velocity by inversion of Rayleigh waves, *Geophysics*, *64*(3), 691–700, doi:10.1190/1.1444578.
- Xu, J., et al. (1987), Formation and evolution of the Tancheng-Lujiang wrench fault system: A major shear system to the northwest of the Pacific Ocean, *Tectonophysics*, *134*(4), 273–310, doi:10.1016/0040-1951(87)90342-8.
- Xu, W.-L., et al. (2006), Mesozoic adakitic rocks from the Xuzhou-Suzhou area, eastern China: Evidence for partial melting of delaminated lower continental crust, *J. Asian Earth Sci.*, *27*(2), 230–240, doi:10.1016/j.jseas.2005.03.005.
- Xu, X., et al. (2008), Re-Os isotopes of sulfides in mantle xenoliths from eastern China: Progressive modification of lithospheric mantle, *Lithos*, *102*(1–2), 43–64, doi:10.1016/j.lithos.2007.06.010.
- Xu, Y.-G. (2001), Thermo-tectonic destruction of the Archaean lithospheric keel beneath the Sino-Korean Craton in China: Evidence, timing and mechanism, *Phys. Chem. Earth*, *26*(9–10), 747–757, doi:10.1016/S1464-1895(01)00124-7.
- Yang, J.-H., et al. (2008), Mesozoic decratonization of the north China block, *Geology*, *36*(6), 467–470, doi:10.1130/G24518A.1.
- Yuan, X. (1996), Velocity structure of the Qinling lithosphere and mushroom cloud model, *Sci. China, Ser. D*, *39*(3), 235–244.
- Zeng, Q.-S., et al. (1989), Crustal deformation in north China during the Holocene (in Chinese), in *Lithospheric Dynamics Atlas of China*, edited by X.-Y. Ma, p. 65, China Cartogr. Publ. House, Beijing.
- Zhai, M.-G., et al. (2004), Geological features of Mesozoic tectonic regime inversion in eastern north China and implication for geodynamics (in Chinese with English abstract), *Earth Sci. Front*, *11*(3), 285–297.
- Zhai, M., et al. (2007), Lower crustal processes leading to Mesozoic lithospheric thinning beneath eastern north China: Underplating, replacement and delamination, *Lithos*, *96*, 36–54, doi:10.1016/j.lithos.2006.09.016.
- Zhang, S.-H., et al. (2009), Contrasting Late Carboniferous and Late Permian–Middle Triassic intrusive suites from the northern margin of the north China craton: Geochronology, petrogenesis, and tectonic implications, *Geol. Soc. Am. Bull.*, *121*(1–2), 181–200.
- Zhang, X.-K., et al. (1996), Fine crustal structure in Yanqing-Huailai region by deep seismic reflection profiling, *Chin. J. Geophys.*, *39*(3), 356–362.
- Zhao, Y., et al. (2004), Yanshanian movement and conversion of tectonic regimes in East Asia (in Chinese with English abstract), *Earth Sci. Front*, *11*(3), 319–328.
- Zheng, J., et al. (2001), Relict refractory mantle beneath the eastern north China block: Significance for lithosphere evolution, *Lithos*, *57*, 43–66, doi:10.1016/S0024-4937(00)00073-6.
- Zheng, J. P., et al. (2007), Mechanism and timing of lithospheric modification and replacement beneath the eastern north China craton: Peridotitic xenoliths from the 100 Ma Fuxin basalts and a regional synthesis, *Geochim. Cosmochim. Acta*, *71*(21), 5203–5225, doi:10.1016/j.gca.2007.07.028.
- Zheng, J. P., et al. (2008), Continental collision and accretion recorded in the deep lithosphere of central China, *Earth Planet. Sci. Lett.*, *269*(3–4), 497–507, doi:10.1016/j.epsl.2008.03.003.
- Zheng, T., et al. (2006), Crust-mantle structure difference across the gravity gradient zone in north China craton: Seismic image of the thinned continental crust, *Phys. Earth Planet. Inter.*, *159*, 43–58, doi:10.1016/j.pepi.2006.05.004.
- Zhou, X., and R. L. Armstrong (1982), Cenozoic volcanic rocks of eastern China secular and geographic trends in chemistry and strontium isotopic composition, *Earth Planet. Sci. Lett.*, *58*(3), 301–329, doi:10.1016/0012-821X(82)90083-8.
- Zhu, L., and R. Zeng (1990), Three-dimensional P wave velocity structure under the Beijing network area, *Acta Geophys. Sin.*, *33*, 267–277.